ACS OMEGA

http://pubs.acs.org/journal/acsodf
Article

Investigation of a Few Noble Metal Oxides with ^{17}O Solid-State NMR Spectroscopy

Yujie Wen, Fang Wang, Heqing Zhu, Changju Yang, Xiaokang Ke, Wei Li, Hua Huo,* and Luming Peng*

Cite This: *ACS Omega* 2025, 10, 13655−13663

Read Online

ACCESS | Metrics & More | Article Recommendations | Supporting Information

ABSTRACT: Noble metal oxides are highly valuable and act as a key component of metal-oxide interfaces in oxide-supported noble metal catalysts, which play a crucial role in modern industrial society. Here, we investigate the structure of four common and stable noble metal oxides using ^{17}O solid-state NMR. The optimal isotopic labeling temperature ensures the highest labeling efficiency while preserving the structure of the oxides. The variation in characteristic signals for each noble metal oxide reveals oxygen species in different chemical environments, while the NMR parameters related to chemical shift anisotropy and quadrupolar interaction obtained from spectral fitting indicate more structural information. DFT calculations are used to assist spectral assignments for various oxygen species. This work serves as a prerequisite for studying solid-state NMR of oxide-supported noble metal catalysts.

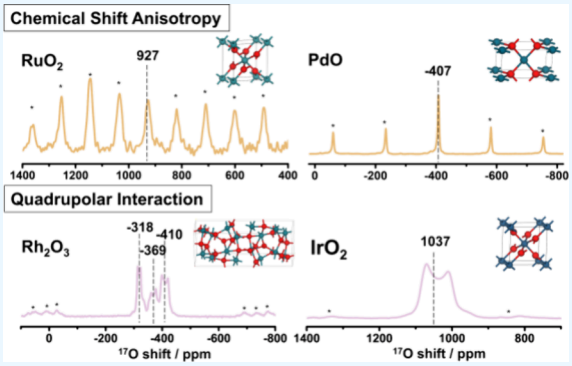

INTRODUCTION

Noble metal oxides, though scarce and costly, are highly valued in modern industrial society.[1−4] Of particular importance are oxide-supported noble metal catalysts, which play a crucial role in various chemical reactions.[5−10] Dispersing these metals as nanoparticles, nanoclusters, or single atoms on supports such as carbon materials, oxides, and zeolites increases the metal−support interfaces, thereby boosting the catalytic activity.[11−14] Moreover, tailoring the metal-oxide interfaces by modifying the composition and coordination environment results in catalysts with adaptable activity and selectivity.[15−17] Since the structure of noble metal oxides is closely related to metal-oxide interfaces,[18,19] obtaining the detailed structural information on these oxides is a critical step to developing the structure−activity relationships as well as the rational design of oxide-supported noble metal catalysts.

Solid-state nuclear magnetic resonance (NMR) is essential for investigating the structure and properties of materials across diverse applications.[20−22] For example, applications of ^{31}P solid-state NMR combined with probe molecules like TMP can provide detailed insights into the exposed facets and oxygen vacancies of oxide surface.[23−25] ^{17}O solid-state NMR is a powerful technique for investigating the local structure of oxides,[26−34] and previous ^{17}O NMR exploration on simple metal oxides lay the foundation for subsequent studies on various complex catalytic systems.[35−38] ^{17}O NMR has been further developed to differentiate among bulk, surface, and interfacial oxygen species in nanomaterials,[39−43] probe the acidity and basicity,[44−47] identify the surface adsorption sites of small molecules,[48−50] and explore the catalytic processes.[51−54] However, to the best of our knowledge, ^{17}O NMR has never been performed to study the oxygen species on the interface in oxide-support noble metal catalysts, which is considered crucial for the performances of the catalysts. It is partially because of the limited work on ^{17}O NMR studies of noble metal oxides. In oxide-supported noble metal catalysts (e.g., M_a/M_bO_y with M_a as the noble metal and M_bO_y as the oxide support), the interfacial species such as M_a-O-M_b are regarded as the active sites.[13,55] The ^{17}O NMR chemical shifts of these interfacial oxygen species are expected to fall between the chemical shifts of the two simple oxides, i.e., noble metal oxide M_aO_x and the support oxide M_bO_y. Therefore, the oxygen species in noble metal oxide M_aO_x are worth investigating in detail with ^{17}O solid-state NMR. Here, we choose several common and stable noble metal oxides—ruthenium(IV) dioxide (RuO_2), palladium(II) oxide (PdO), rhodium(III) oxide (Rh_2O_3), and iridium(IV) dioxide (IrO_2). PdO and Rh_2O_3 have not been investigated by ^{17}O NMR before, while there is very limited ^{17}O NMR data of RuO_2[56] and IrO_2.[57] The results should help to develop a deeper understanding of noble metal

Received: February 1, 2025
Revised: March 12, 2025
Accepted: March 18, 2025
Published: March 25, 2025

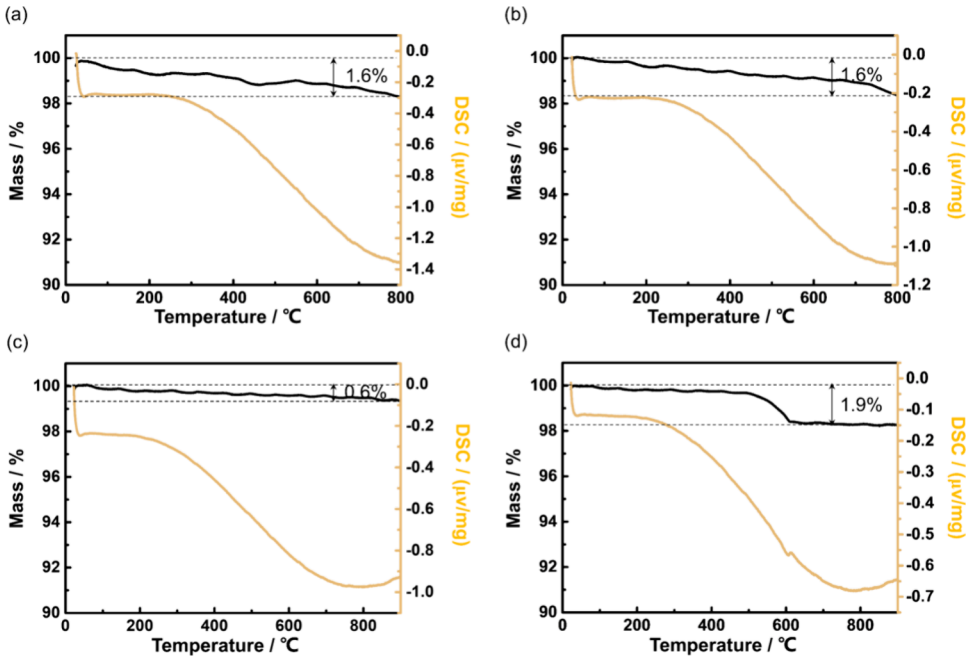

Figure 1. TGA-DSC analysis of (a) RuO_2, (b) PdO, (c) Rh_2O_3, and (d) IrO_2.

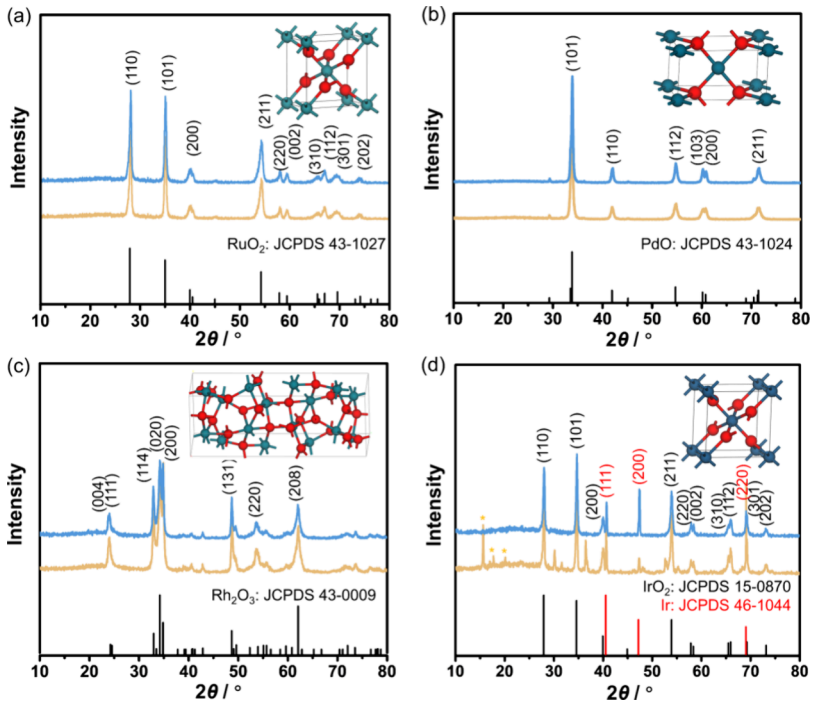

Figure 2. XRD patterns of (a) RuO_2, (b) PdO, (c) Rh_2O_3, and (d) IrO_2 before (yellow) and after (blue) high-temperature ^{17}O isotopic labeling, with JCPDS card data shown below. The insets display the unit cells of the oxides. Peacock blue and red spheres represent the noble metal and oxygen atoms, respectively.

oxides and further research into oxide-supported noble metal catalysts.

RESULTS

We first conducted thermogravimetric analysis and differential scanning calorimetry (TGA-DSC) tests on RuO_2, PdO, Rh_2O_3, and IrO_2 in an air atmosphere to follow the possible changes of each oxide as a function of temperature (Figure 1). RuO_2 shows a slight mass loss of 1.6% from room temperature to 800 °C. Its DSC curve exhibits only one weak and broad endothermic peak, which can be attributed to the removal of surface water molecules and surface hydroxyl (Figure 1a).[58,59] Similarly, PdO and Rh_2O_3 display a mass loss of 1.6 and 0.6% in the tested temperature range, respectively (Figure 1b,c).[58] In addition to the minor weight loss at relatively low temperatures, IrO_2 shows a more significant loss beginning at around 510 °C, with an overall loss of 1.9% (Figure 1d). XRD analysis reveals impurity diffraction peaks in the pristine iridium oxide sample, which disappears after high-temperature

https://doi.org/10.1021/acsomega.5c00998
ACS Omega 2025, 10, 13655−13663

calcination (Figure 2d). Therefore, the additional mass loss is attributed to the removal of these impurities.[58]

Efficient ^{17}O isotopic labeling is crucial for obtaining high-quality ^{17}O NMR spectra.[32,35,36] This process typically requires sufficiently high temperatures to ensure labeling efficiency, but excessive temperatures may alter the oxide structures. To ensure both isotopic labeling efficiency and structural stability, we selected appropriate isotopic labeling temperatures based on the TGA-DSC results (Figure 1): 700 °C for RuO_2, 700 °C for PdO, 800 °C for Rh_2O_3, and 800 °C for IrO_2.

X-ray diffraction (XRD) analysis of the oxides is shown in Figure 2, yellow lines. The crystal structure of the RuO_2 belongs to the tetragonal system with space group $P4_2/mnm$ (Figure 2a), in which Ru^{4+} is bonded to six equivalent O^{2-} atoms to form RuO_6 octahedra while O^{2-} is bonded in a trigonal planar geometry to three equivalent Ru^{4+} atoms. Figure 2b shows that the crystal structure of the PdO belongs to the tetragonal system with space group $P4_2/mmc$. Pd^{2+} is bonded in a square planar geometry to four equivalent O^{2-} atoms and O^{2-} is bonded to four equivalent Pd^{2+} atoms to form an OPd_4 tetrahedra. The crystal structure of the Rh_2O_3 belongs to the orthorhombic system with space group *Pbca*, featuring two types of six-coordinated Rh^{3+} and three inequivalent O^{2-} sites (Figure 2c). Each O^{2-} is bonded to four Rh^{3+} ions with varying Rh−O bond distances and Rh−O−Rh bond angles. Figure 2d exhibits the crystal structure of IrO_2 (tetragonal $P4_2/mnm$ space group). In this structure, each Ir^{4+} is surrounded by equivalent O^{2-}, forming an octahedral coordination, while each O^{2-} is coordinated with three equivalent Ir^{4+}.

To further ensure that the oxides maintain consistent phase structures before and after heating for isotopic labeling, X-ray diffraction (XRD) was conducted on the oxides after being heated in an $^{17}O_2$ atmosphere (Figure 2, blue lines). The diffraction peaks for the oxides are found to be nearly identical. These results guarantee that the obtained NMR spectra can accurately reflect the original chemical environment of oxygen species in the oxides. The XRD pattern of IrO_2 shows distinct peaks corresponding to metallic iridium, matching JCPDS 46-1044, with 2θ values of 40.7°, 47.3°, and 69.1°, associated with the (111), (200), and (220) crystal planes, respectively (Figure 2d). These peaks become sharper after the high-temperature treatment, indicating that the metallic iridium may have undergone grain growth. Moreover, the XRD reflections marked with asterisks at 2θ = 15.5°, 17.7°, and 20.1°, which should arise from impurities, disappear after high-temperature treatment, indicating the removal of these unwanted species. This observation aligns with the slight mass loss starting around 510 °C, as detected in the TGA-DSC analysis (Figure 1d). The results of TGA-DSC and XRD ensure that the structures of the oxides do not change during the high temperature isotopic labeling process before the acquisition of high-quality ^{17}O NMR spectra.

Figure 3 shows the ^{17}O NMR spectra of RuO_2 enriched with $^{17}O_2$ at 700 °C, acquired using the parameters listed in Table S1. A peak centered at 927 ppm with strong sidebands is observed at an external magnetic field of 20 T (Figure 3a). Variable spinning speed experiment confirms that the center band resonates at 927 ppm (Figure 3b). The frequency of the peak remains at 927 ppm at 9.4 T, indicating very small quadrupolar interactions (Figure 3c), therefore the quadrupolar interaction is not considered in the following simulations for RuO_2. The peak at 927 ppm can be attributed

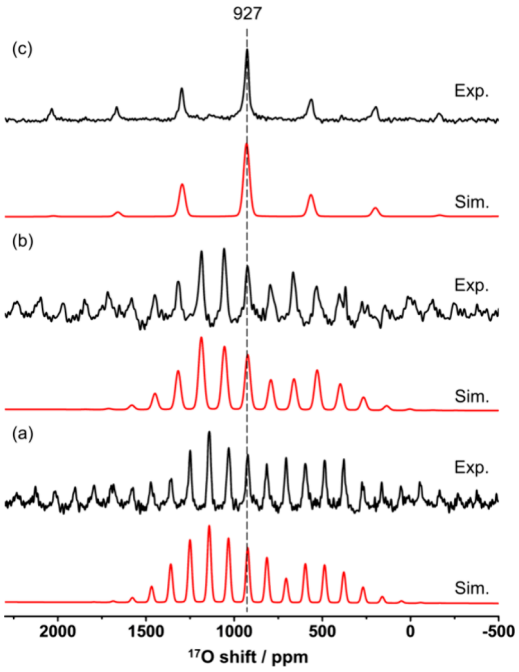

Figure 3. Experimental (black) and simulated (red) ^{17}O solid-state NMR spectra of RuO_2. The ^{17}O NMR measurements were recorded at different external fields and spinning rates: (a) 20 T, 12.5 kHz; (b) 20 T, 15 kHz; and (c) 9.4 T, 20 kHz. ^{1}H decoupling was applied during acquisition and a recycle delay of 4 s was used. NMR parameters used for simulation are shown in Table 1.

to the oxygen species in the bulk of RuO_2, closely aligning with the NMR shift obtained in the RuO_2/Li battery system,[56] and this observation is in agreement with the single oxygen site in the structure (Figure 2a). The spectra show significant spinning sidebands and the simulated spectra considering chemical shift anisotropy (CSA) are presented in Figure 3 (red lines), with the NMR parameters used for simulation, including isotropic chemical shift (δ_{iso}), CSA ($\Delta\sigma$), and the asymmetry parameter of CSA (η_{CSA}), shown in Table 1. The fitting shows that the oxygen species are subjected to strong CSA with a $\Delta\sigma$ of −730 ppm and an η_{CSA} of 0.5. DFT calculations of NMR parameters were performed to compare with the experimental data (Tables 1 and S2). A difference of approximately 4 ppm in centers of gravity (δ_{CG}) between 9.4 and 20 T is expected according to a calculated quadrupole coupling constant (C_Q) of 1.5 MHz, however, no difference is observed in our experimental data (Figure 3), indicating that the calculated C_Q for RuO_2 is larger. The calculated $\Delta\sigma$ and η_{CSA} are −783 ppm and 0.36, respectively, which are similar to our experimental observation. The differences between calculated and experimental values may be ascribed to the fact that DFT calculations are performed using crystal structures at 0 K.

Figure 4 shows the ^{17}O NMR spectra of PdO enriched with $^{17}O_2$ at 700 °C, acquired using the parameters listed in Table S1. A sharp peak at −407 ppm can be observed at different external magnetic fields, suggesting weak quadrupolar interactions and this single peak is consistent with the single environment of oxygen in the PdO structure (Figure 2b). Similar to the case for RuO_2, quadrupolar interaction is not considered in the spectral simulations, and the fitting results are shown in Table 1 and Figure 4 (red lines). Clearly, the

https://doi.org/10.1021/acsomega.5c00998
ACS Omega 2025, 10, 13655−13663

Table 1. NMR Parameters Obtained by Simulating Experimental ^{17}O MAS NMR Spectra of RuO_2 and PdO in Comparison to the NMR Parameters According to DFT Calculations

		δ_{iso}/ppm	C_Q/MHz	asymmetry parameter (η_Q)	$\Delta\sigma$/ppm	η_{CSA}
RuO_2	Exp.	927 (±1)	~0.6[a]		−730 (±50)	0.5 (±0.1)
	Calc.		1.5	0.87	−783	0.36
PdO	Exp.	−407 (±1)	~0.6[a]		330 (±70)	0.9 (±0.1)
	Calc.		1.1	0.03	236	0.31

[a]The C_Q values are estimated based in Figure S1.[28,60]

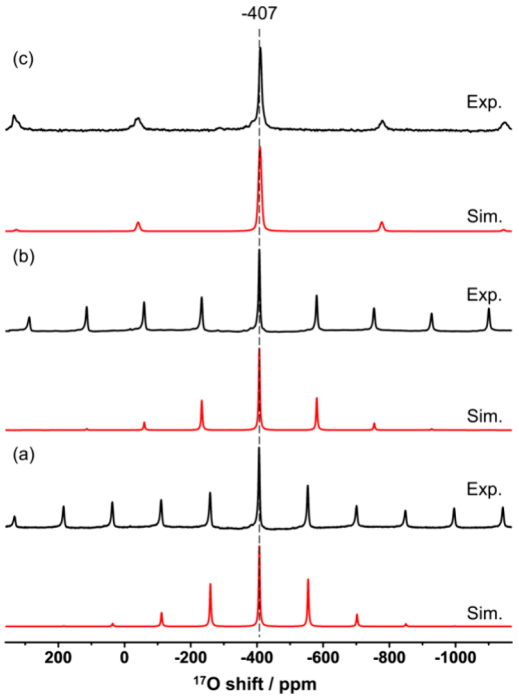

Figure 4. Experimental (black) and simulated (red) ^{17}O solid-state NMR spectra of PdO. The ^{17}O NMR measurements were recorded at different external fields and spinning rates: (a) 20 T, 17 kHz; (b) 20 T, 20 kHz; and (c) 9.4 T, 20 kHz. ^{1}H decoupling was applied during acquisition and a recycle delay of 4 s was used. NMR parameters used for simulation are shown in Table 1.

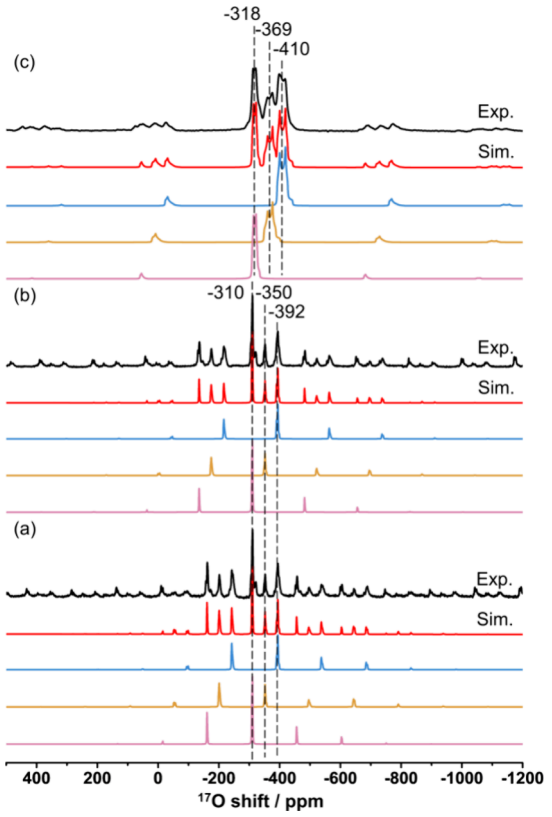

Figure 5. Experimental (black) and simulated (colored) ^{17}O solid-state NMR spectra of Rh_2O_3. The ^{17}O NMR measurements were recorded at different external fields and spinning rates: (a) 20 T, 17 kHz; (b) 20 T, 20 kHz; and (c) 9.4 T, 20 kHz. ^{1}H decoupling was applied during acquisition and a recycle delay of 4 s was used. NMR parameters used for simulation are shown in Table 2.

oxygen species in PdO exhibit significantly weaker CSA compared to RuO_2.

Figure 5 presents the ^{17}O NMR spectra of Rh_2O_3 enriched with $^{17}O_2$ at 800 °C, acquired using the parameters listed in Table S1. By comparing the spectra obtained with different spinning speeds at 20 T, it is clear that three resonances centered at −310, −350, and −392 ppm are observed for Rh_2O_3 (Figure 5a,b). Notably, ^{17}O NMR signals obtained at 9.4 T exhibit more pronounced second order quadrupolar line broadening, and shift toward lower frequencies (Figure 5c). These results indicate relatively large quadrupolar interactions for the oxygen species in the bulk part of Rh_2O_3 and the number of different signals is consistent with the structure (Figure 2c). Although the coordination numbers of these three oxygen species are the same, the variation in Rh−O bond lengths and Rh−O−Rh bond angles can lead to differences in their NMR parameters (Figure S2 and Table S3). The NMR spectra are simulated considering both quadrupolar interaction and CSA (Figure 5, colored lines), and the corresponding parameters are extracted (Table 2). The values of C_Q are 2.3, 3.3, and 3.3 MHz, with $\Delta\sigma$ of −280, −450, and −355 ppm for the peaks with δ_{iso} of −308, −345, and −387 ppm, respectively.

The ranges of Rh−O−Rh bond angles for O2 and O3 sites are very similar, while O1 has a smaller variation in bond angles (Table S3). Therefore, the peak with the smallest value of C_Q (2.3 MHz) and $\Delta\sigma$ (−280 ppm) is tentatively assigned to O1 (δ_{iso} = −308 ppm) (Table 2). Rh−O bond length distribution is wider for O2 than O3 (Figure S2), thus the resonances with a larger $\Delta\sigma$ (−450 ppm) and a smaller $\Delta\sigma$ (−355 ppm) are tentatively assigned to O2 (δ_{iso} = −345 ppm) and O3 (δ_{iso} = −387 ppm), respectively (Table 2). The DFT calculations for Rh_2O_3 indicate that O1, O2 and O3 are associated with C_Qs of 2.5, 3.4, and 3.4 MHz (Tables 2 and S4), which agree well with the experimental data. The calculated values of $\Delta\sigma$ for O1, O2, and O3 are −144, −299, and −281 ppm, respectively, which show some differences compared to the experimental values but the sizes of calculated $\Delta\sigma$ follow the same order compared to the experimental data. The DFT calculation results confirm the spectral assignments. Again, these results demonstrate the

https://doi.org/10.1021/acsomega.5c00998
ACS Omega 2025, 10, 13655−13663

Table 2. NMR Parameters Obtained by Simulating Experimental ^{17}O MAS NMR Spectra of Rh_2O_3 and IrO_2 in Comparison to the Calculated NMR Parameters, and the δ_{CG}s Obtained at 9.4 and 20 T

		δ_{iso}/ppm	C_Q/MHz	η_Q	$\Delta\sigma$/ppm	η_{CSA}	δ_{CG}/ppm 9.4 T	δ_{CG}/ppm 20 T	assignment
Rh_2O_3	Exp.	−308 (±2)	2.3 (±0.2)	0.2 (±0.1)	−280 (±60)	0.2 (±0.1)	−318	−310	O1
	Calc.		2.5	0.12	−144	0.67			
	Exp.	−345 (±2)	3.3 (±0.2)	0.4 (±0.1)	−450 (±60)	0.2 (±0.1)	−369	−350	O2
	Calc.		3.4	0.30	−299	0.68			
	Exp.	−387 (±2)	3.3 (±0.2)	0.2 (±0.1)	−355 (±40)	0.4 (±0.1)	−410	−392	O3
	Calc.		3.4	0.12	−281	0.35			
IrO_2	Exp.	1102 (±4)	5.6 (±0.3)	0.2 (±0.1)			1037	1088	
	Calc.		6.2	0.18					

strong influences of bond lengths and bond angles on the NMR parameters of oxygen ions.

The ^{17}O NMR spectrum of IrO_2, enriched with $^{17}O_2$ at 800 °C at 20 T and acquired using the parameters listed in Table S1, shows a single signal (Figure 6a,b). This resonance shows a characteristic second-order quadrupolar line shape and shifts to lower frequencies at a lower magnetic field strength (9.4 T, Figure 6c), similar to Rh_2O_3 (Figure 5). This data indicates the presence of only one type of oxygen species, consistent with the number of oxygen species in the structure (Figure 2d). The intensities of the low-order spinning sidebands of IrO_2 are small and very similar (Figure 6), implying very small CSA. Therefore, CSA is not considered in the following simulation. At the same time, the much larger line width of the center band with a characteristic second order quadrupolar line shape (e.g., the data obtained at 9.4 T) indicates a stronger quadrupolar interaction compared to Rh_2O_3. The simulated spectra are presented in Figure 6 (red lines), with the NMR parameters, including a large C_Q of 5.6 MHz, obtained by numerical simulation (Table 2). The calculated C_Q and η_Q for IrO_2 are 6.2 MHz and 0.18, respectively, consistent with the experimental results.

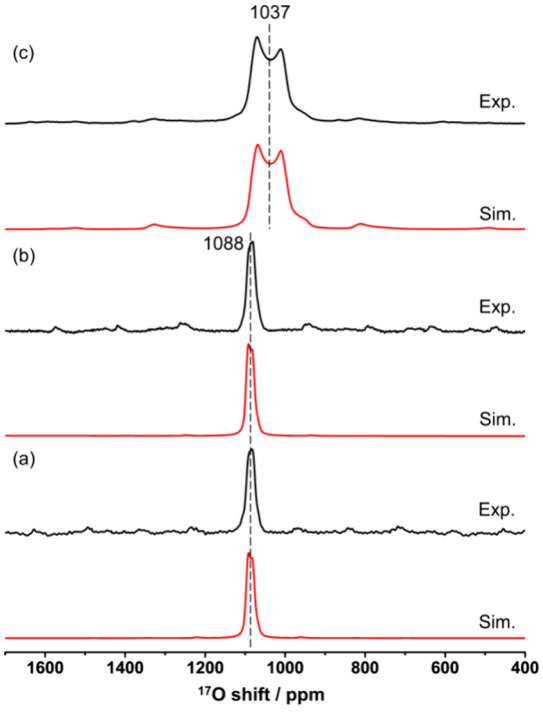

Figure 6. Experimental (black) and simulated (red) ^{17}O solid-state NMR spectra of IrO_2. The ^{17}O NMR measurements were recorded at different external fields and spinning rates: (a) 20 T, 15 kHz; (b) 20 T, 18 kHz; and (c) 9.4 T, 14 kHz. ^1H decoupling was applied during acquisition and a recycle delay of 4 s was used. NMR parameters used for simulation are shown in Table 2.

DISCUSSION

By comparing the NMR parameters obtained in this study to previous work, attempts were made to explore the relationship between ^{17}O NMR parameters and structural factors (i.e., coordination species, coordination number, bond length, and bond angle) (Table S5). Previous research has shown that for chemically similar metals in the same main group, such as BeO, MgO, CaO, SrO, and BaO, there is a linear relationship between bond length and chemical shift.[28] Studies on silicates have also shown that the chemical shift of oxygen species increases with the elongation of the Si−O bond length, while the values of C_Q and η_Q of oxygen sites are closely related to the Si−O−Si bond angles and/or Si−O bond distances.[61−65] However, these kinds of relatively simple correlations are not found in oxides like Cu_2O, Ag_2O, Sc_2O_3, and Y_2O_3.[29,66] In some simple oxides, such as monoclinic ZrO_2, there are two distinct chemical environments for the oxygen species, with significant variations in both bond lengths and bond angles. In such cases, it is not sufficient to describe the changes in chemical shifts using just one variable, such as bond length or bond angle. Instead, correlations between coordination number and chemical shift can be observed.[29,67] These findings suggest that the NMR parameters of the ^{17}O signal are influenced by various factors, and establishing a relationship between the structure and NMR parameters may not be straightforward.

In this study, RuO_2 and IrO_2 share the same crystal structure and space group, where O^{2-} ions are bonded in a trigonal planar geometry to three equivalent M^{4+} atoms. Despite this similarity, the oxygen species in RuO_2 and IrO_2 exhibit significant differences in chemical shifts, CSA parameters, and quadrupolar coupling constants, highlighting the influence of coordination species. For oxides with different structures, e.g., RuO_2 and PdO, the differences in NMR parameters are attributed to both the change in the coordinating metal atoms and the variation in oxygen coordination numbers (three-coordinated in RuO_2 and four-coordinated in PdO). Different coordination numbers significantly alter the local geometry, leading to distinct M-O bond lengths and bond angles, which in turn affect the NMR parameters. In Rh_2O_3, three distinct tetrahedral ORh_4 species are observed. Among these species, O1 has a relatively uniform bond angle distribution compared to O2 and O3, resulting in a smaller C_Q value. O2 and O3

https://doi.org/10.1021/acsomega.5c00998
ACS Omega 2025, 10, 13655−13663

share similar bond angle distributions and thus exhibit comparable C_Qs. However, O2 has a broader bond length distribution than O3, leading to a larger $\Delta\sigma$. This differentiation between O1, O2, and O3 underscores the significant effects of bond angles and bond lengths on NMR parameters. The differences between the calculated CSA and the experimentally obtained values can be attributed to several possible factors. First, spin−orbit coupling is not considered in the calculations presented in Tables 1 and 2, while its effects can be complex and vary across different oxides (see Table S2 for the results incorporating spin−orbit coupling).[68−70] Second, the CSA values may be overestimated due to contribution from satellite transitions (see Figure S3 and Table S6 for the attempts to eliminate these contributions). Third, the Euler angles are not accounted for in the simultaneous fitting of quadrupolar and CSA effects.[71,72] Finally, the paramagnetic effects may originate from the mixing of low-lying excited electronic states with the ground state, potentially influencing chemical shielding parameters.[73−76]

CONCLUSIONS

In summary, by isotopically labeling noble metal oxides with $^{17}O_2$ at appropriate temperatures, we identify distinct ^{17}O NMR signals that reveal significant variations in chemical environments and provide valuable structural information. The NMR spectra of RuO_2, PdO, Rh_2O_3, and IrO_2, which exhibit pronounced CSA and quadrupolar effects, are fitted to extract the related NMR parameters for the oxygen species. The DFT results confirm the spectral assignments of the various oxygen species. This demonstrates that solid-state NMR is highly sensitive to the coordination environment of oxides. Although this study primarily focuses on the bulk structures of noble metal oxides, their surface and interfaces, which either constitute or are related to a significant portion of the oxide-supported noble metal catalysts, are the key to related catalytic processes. Future studies of these species should provide crucial structural information on the active sites and help establish structure−property relationships.

METHODS

All noble metal oxides were purchased from Aladdin Scientific Corporation and used as received.

Characterization. Thermogravimetric analysis and differential scanning calorimetry (TGA-DSC) test of the sample were performed using a STA449F3 analyzer with a rate of 10 °C min^{-1} in air. Power X-ray diffraction (XRD) was used to identify the crystalline phase structure conducted at Philips X'pert Pro X-ray diffractometer with a Cu $k\alpha$ (λ = 0.15418 nm) radiation. The operating voltage and current were set to 40 kV and 40 mA, respectively, with a scanning speed of 2 °/min.

The catalysts were isotopically labeled using commercial $^{17}O_2$ gas (90% ^{17}O, Cambridge Isotope Laboratories). The enrichment process was carried out in a quartz tube with a radius of 6 mm. The heating rate was set to 10 °C per minute until the specified enrichment temperature was reached, after which the tube was held at that temperature for 24 h. In a typical process, RuO_2 (150 mg) was placed in a quartz tube and heated at 700 °C for 1 h under vacuum to remove the physically adsorbed water and impurities. After cooling to room temperature, $^{17}O_2$ was introduced into the quartz tube, which was then sealed and allowed to exchange at 700 °C for 24 h. Other noble metal oxides were isotopic labeled in the same way but using different temperatures (700 °C for PdO, 800 °C for Rh_2O_3, and 800 °C for IrO_2).

^{17}O solid-state nuclear magnetic resonance (NMR) experiments were conducted on a 9.4 T Bruker Avance III spectrometer equipped at a Larmor frequency of 54.2 MHz with a 3.2 mm HX probe and a 20 T Bruker Avance NEO spectrometer at a Larmor frequency of 115.2 MHz with a 3.2 mm HX MAS probe. All samples were packed into laser-marked rotors in an N_2 glovebox. The chemical shift of ^{17}O was referenced using H_2O at 0.0 ppm. Dmfit package was used to simulate all ^{17}O NMR spectra.[77]

DFT Calculation. The calculations were performed using the *Vienna Ab initio Simulation Package* (*VASP*),[78] applying the generalized gradient approximation with the Perdew−Burke−Ernzerhof (PBE) functional.[79] The plane-wave kinetic energy cutoff was set at 500 eV.[80] Geometry optimizations were finished when the Hellman-Feynman force on each relaxed ion fell below 0.02 eV·$Å^{-1}$. The convergence thresholds were set at 10^{-5} eV for geometric optimizations and 10^{-8} eV for electric field gradients (EFG).[39] We obtained optimized lattice parameters of a = 4.540 Å and c = 3.1841 Å, a = 3.110 Å and c = 5.367 Å, a = 5.207 Å and c = 14.865 Å, a = 4.528 Å and c = 3.121 Å for bulk IrO_2, PdO, Rh_2O_3, RuO_2, with a corresponding 6 × 6 × 8, 8 × 8 × 5, 5 × 5 × 2, and 6 × 6 × 8 k-point mesh, respectively. The ^{17}O NMR parameter calculations for the P (2 × 2 × 2) supercell of the oxides were carried out in accordance with the methodology outlined in our previous work.[39]

To calculate the quadrupole coupling constant (C_Q) and asymmetry parameter (η_Q), we used the following equations:

$$C_Q = \frac{eQV_{ZZ}}{h}$$

$$\eta_Q = \frac{V_{XX} - V_{YY}}{V_{ZZ}}$$

where h is the Planck constant, e is the absolute value of the electron charge, and V_{ii} (ii = XX, YY, or ZZ) are the eigenvalues of the EFG tensor with $|V_{ZZ}| > |V_{YY}| > |V_{XX}|$. To calculate the quadrupolar parameters (C_Q) for ^{17}O, the experimental quadrupole moment (Q) of −0.02558 barns[81] was used.

To calculate the anisotropy ($\Delta\sigma$) and asymmetry parameter (η_{CSA}), we used the following equations:

$$\delta_{iso} = (\delta_{XX} + \delta_{YY} + \delta_{YY})/3$$

$$\Delta\sigma = \delta_{ZZ} - (\delta_{XX} + \delta_{YY})/2$$

$$\eta_{CSA} = \frac{(\delta_{YY} - \delta_{XX})}{(\delta_{ZZ} - \delta_{iso})}$$

where δ_{ii} (ii = XX, YY, or ZZ) are the principal components of the chemical shift tensor with $|\delta_{ZZ} - \delta_{iso}| \geq |\delta_{XX} - \delta_{iso}| \geq |\delta_{YY} - \delta_{iso}|$.

ASSOCIATED CONTENT

Supporting Information

The Supporting Information is available free of charge at https://pubs.acs.org/doi/10.1021/acsomega.5c00998.

https://doi.org/10.1021/acsomega.5c00998
ACS Omega 2025, 10, 13655−13663

Details on DFT calculations using CASTEP, NMR acquisition parameters, additional NMR data, experimentally obtained and calculated NMR parameters, and the local structure of Rh_2O_3 (PDF)

AUTHOR INFORMATION

Corresponding Authors

Hua Huo − *Key Laboratory of Materials for New Energy Conversion and Storage Ministry of Industry and Information Technology, School of Chemistry and Chemical Engineering, Harbin Institute of Technology, Harbin 150001, China;* orcid.org/0000-0002-2790-8225; Email: huohua@hit.edu.cn

Luming Peng − *Key Laboratory of Mesoscopic Chemistry of MOE, School of Chemistry and Chemical Engineering, Nanjing University, Nanjing 210023, China; Jiangsu Key Laboratory of Vehicle Emissions Control, Nanjing University, Nanjing 210093, China; Frontiers Science Center for Critical Earth Material Cycling (FSC-CEMaC), Nanjing University, Nanjing, Jiangsu 210023, China;* orcid.org/0000-0003-1935-1620; Email: luming@nju.edu.cn

Authors

Yujie Wen − *Key Laboratory of Mesoscopic Chemistry of MOE, School of Chemistry and Chemical Engineering, Nanjing University, Nanjing 210023, China;* orcid.org/0009-0001-2250-8396

Fang Wang − *Key Laboratory of Mesoscopic Chemistry of MOE, School of Chemistry and Chemical Engineering, Nanjing University, Nanjing 210023, China*

Heqing Zhu − *Key Laboratory of Mesoscopic Chemistry of MOE, School of Chemistry and Chemical Engineering, Nanjing University, Nanjing 210023, China; Department of Chemistry, University of California, Berkeley, Berkeley, California 94720, United States; Materials Sciences Division, Lawrence Berkeley National Laboratory, Berkeley, California 94720, United States*

Changju Yang − *Key Laboratory of Mesoscopic Chemistry of MOE, School of Chemistry and Chemical Engineering, Nanjing University, Nanjing 210023, China;* orcid.org/0009-0002-0802-5088

Xiaokang Ke − *Key Laboratory of Mesoscopic Chemistry of MOE, School of Chemistry and Chemical Engineering, Nanjing University, Nanjing 210023, China*

Wei Li − *Key Laboratory of Mesoscopic Chemistry of MOE, School of Chemistry and Chemical Engineering, Nanjing University, Nanjing 210023, China;* orcid.org/0000-0001-7801-3643

Complete contact information is available at: https://pubs.acs.org/10.1021/acsomega.5c00998

Author Contributions

Y.W., H.Z. X.K., H.H., and L.P. performed ^{17}O isotope enrichment, collected as well as analyzed the NMR spectra; Y.W. and C.Y. conducted other characterizations of the catalysts and analyzed the results; F.W. and W.L. conducted the DFT calculations; L.P. conceived the idea, designed the study and coordinated the project. Y.W. and L.P. wrote the manuscript, and all authors discussed the experiments and final manuscript.

Notes

The authors declare no competing financial interest.

ACKNOWLEDGMENTS

This work was supported by the National Natural Science Foundation of China (NSFC) (22472075, 22075064, 22272075, W2421041, 21972066, and 91745202), and NSFC - Royal Society Joint Program (21661130149). L.P. thanks the Royal Society and Newton Fund for a Royal Society - Newton Advanced Fellowship. This work was also supported by the Research Funds for the Frontiers Science Center for Critical Earth Material Cycling, Nanjing University, and a Project Funded by the Priority Academic Program Development of Jiangsu Higher Education Institutions. We thank Prof. Fred Blanc at the University of Liverpool for the assistance in obtaining the high field NMR data and invaluable discussions. We are grateful to the High Performance Computing Center of Nanjing University for doing the numerical calculations in this paper on its blade cluster system.

REFERENCES

(1) Wang, Z.; Jiang, H.; Jang, M. H.; Lin, P.; Ribbe, A.; Xia, Q.; Yang, J. J. Electrochemical metallization switching with a platinum group metal in different oxides. *Nanoscale* **2016**, *8*, 14023−14030.

(2) Hughes, A. E.; Haque, N.; Northey, S. A.; Giddey, S. Platinum group metals: A review of resources, production and usage with a focus on catalysts. *Resources* **2021**, *10*, 93.

(3) Cui, C.-H.; Yu, S.-H. Engineering interface and surface of noble metal nanoparticle nanotubes toward enhanced catalytic activity for fuel cell applications. *Acc. Chem. Res.* **2013**, *46*, 1427−1437.

(4) Fan, Z.; Zhang, H. Template synthesis of noble metal nanocrystals with unusual crystal structures and their catalytic applications. *Acc. Chem. Res.* **2016**, *49*, 2841−2850.

(5) Daubignard, J.; Detz, R. J.; Jans, A. C. H.; de Bruin, B.; Reek, J. N. H. Rational optimization of supramolecular catalysts for the rhodium-catalyzed asymmetric hydrogenation reaction. *Angew. Chem., Int. Ed.* **2017**, *56*, 13056−13060.

(6) Stepic, R.; Wick, C. R.; Strobel, V.; Berger, D.; Vucemilovic-Alagic, N.; Haumann, M.; Wasserscheid, P.; Smith, A. S.; Smith, D. M. Mechanism of the water-gas shift reaction catalyzed by efficient ruthenium-based catalysts: A computational and experimental study. *Angew. Chem., Int. Ed.* **2019**, *58*, 741−745.

(7) Drake, T.; Ji, P.; Lin, W. Site isolation in metal−organic frameworks enables novel transition metal catalysis. *Acc. Chem. Res.* **2018**, *51*, 2129−2138.

(8) Chen, S.; Wojcieszak, R.; Dumeignil, F.; Marceau, E.; Royer, S. How catalysts and experimental conditions determine the selective hydroconversion of furfural and 5-hydroxymethylfurfural. *Chem. Rev.* **2018**, *118*, 11023−11117.

(9) Tian, S.; Gong, W.; Chen, W.; Lin, N.; Zhu, Y.; Feng, Q.; Xu, Q.; Fu, Q.; Chen, C.; Luo, J.; Yan, W.; Zhao, H.; Wang, D.; Li, Y. Regulating the catalytic performance of single-atomic-site Ir catalyst for biomass conversion by metal-support interactions. *ACS Catal.* **2019**, *9*, 5223−5230.

(10) He, T.; Kong, X.-J.; Zhou, J.; Zhao, C.; Wang, K.; Wu, X.-Q.; Lv, X.-L.; Si, G.-R.; Li, J.-R.; Nie, Z.-R. A practice of reticular chemistry: Construction of a robust mesoporous palladium metal-organic framework via metal metathesis. *J. Am. Chem. Soc.* **2021**, *143*, 9901−9911.

(11) Xia, Y.; Yang, H.; Campbell, C. T. Nanoparticles for catalysis. *Acc. Chem. Res.* **2013**, *46*, 1671−1672.

(12) Feng, J.; He, Y.; Liu, Y.; Du, Y.; Li, D. Supported catalysts based on layered double hydroxides for catalytic oxidation and hydrogenation: general functionality and promising application prospects. *Chem. Soc. Rev.* **2015**, *44*, 5291−5319.

(13) Liu, L.; Corma, A. Metal catalysts for heterogeneous catalysis: From single atoms to nanoclusters and nanoparticles. *Chem. Rev.* **2018**, *118*, 4981−5079.

(14) Babucci, M.; Guntida, A.; Gates, B. C. Atomically dispersed metals on well-defined supports including zeolites and metal-organic

https://doi.org/10.1021/acsomega.5c00998
ACS Omega 2025, 10, 13655−13663

frameworks: Structure, bonding, reactivity, and catalysis. *Chem. Rev.* **2020**, *120*, 11956−11985.
(15) Gao, W.; Hood, Z. D.; Chi, M. Interfaces in heterogeneous catalysts: Advancing mechanistic understanding through atomic-scale measurements. *Acc. Chem. Res.* **2017**, *50*, 787−795.
(16) Liu, P.; Qin, R.; Fu, G.; Zheng, N. Surface coordination chemistry of metal nanomaterials. *J. Am. Chem. Soc.* **2017**, *139*, 2122−2131.
(17) van Deelen, T. W.; Mejía, C. H.; de Jong, K. P. Control of metal-support interactions in heterogeneous catalysts to enhance activity and selectivity. *Nat. Catal.* **2019**, *2*, 955−970.
(18) Du, X.; Tang, H.; Qiao, B. Oxidative strong metal-support interactions. *Catalysts* **2021**, *11*, 896.
(19) Wu, G.; Liu, Y.; Wang, J. Oxidative-atmosphere-induced strong metal-support interaction and its catalytic application. *Acc. Chem. Res.* **2023**, *56*, 911−923.
(20) Zhang, W.; Xu, S.; Han, X.; Bao, X. In situ solid-state NMR for heterogeneous catalysis: a joint experimental and theoretical approach. *Chem. Soc. Rev.* **2012**, *41*, 192−210.
(21) Ashbrook, S. E.; Griffin, J. M.; Johnston, K. E. Recent advances in solid-state nuclear magnetic resonance spectroscopy. *Annu. Rev. Anal. Chem.* **2018**, *11*, 485−508.
(22) Xu, J.; Wang, Q.; Deng, F. Metal active sites and their catalytic functions in zeolites: Insights from solid-state NMR spectroscopy. *Acc. Chem. Res.* **2019**, *52*, 2179−2189.
(23) Yi, X.; Peng, Y.-K.; Chen, W.; Liu, Z.; Zheng, A. Surface fingerprinting of faceted metal oxides and porous zeolite catalysts by probe-assisted solid-state NMR approaches. *Acc. Chem. Res.* **2021**, *54*, 2421−2433.
(24) Gao, P.; Ji, Y.; Hou, G. Solid-state nuclear magnetic resonance spectroscopy for surface characterization of metal oxide nanoparticles: State of the art and perspectives. *J. Am. Chem. Soc.* **2025**, *147*, 2919−2937.
(25) Peng, Y.-K.; Ye, L.; Qu, J.; Zhang, L.; Fu, Y.; Teixeira, I. F.; McPherson, I. J.; He, H.; Tsang, S. C. E. Trimethylphosphine-assisted surface fingerprinting of metal oxide nanoparticle by ^{31}P solid-state NMR: A zinc oxide case study. *J. Am. Chem. Soc.* **2016**, *138*, 2225−2234.
(26) Schramm, S.; Oldfield, E. High-resolution oxygen-17 NMR of solids. *J. Am. Chem. Soc.* **1984**, *106*, 2502−2506.
(27) Yang, S.; Park, K. D.; Oldfield, E. Oxygen-17 labeling of oxides and zeolites. *J. Am. Chem. Soc.* **1989**, *111*, 7278−7279.
(28) Turner, G. L.; Chung, S. E.; Oldfield, E. Solid-state oxygen-17 nuclear magnetic resonance spectroscopic study of the group II oxides. *J. Magn. Reson.* **1985**, *64*, 316−324.
(29) Bastow, T. J.; Stuart, S. N. ^{17}O NMR in simple oxides. *Chem. Phys.* **1990**, *143*, 459−467.
(30) Gerothanassis, I. P. Oxygen-17 NMR spectroscopy: Basic principles and applications (Part I). *Prog. Nucl. Magn. Reson. Spectrosc.* **2010**, *56*, 95−197.
(31) Xia, X.-F.; Zhang, W.-J.; Lin, Z.-Y.; Ke, X.-K.; Wen, Y.-J.; Wang, F.; Chen, J.-C.; Peng, L.-M. Solid-state NMR studies on the surface structure and properties of oxide nanomaterials. *Chin. J. Magn. Reson.* **2021**, *38*, 533−542.
(32) Xia, X.; Zhu, L.; Tang, W.; Peng, L.; Chen, J. A review of ^{17}O isotopic labeling techniques for solid-state NMR structural studies of metal oxides in lithium-ion batteries. *Magn. Reson. Lett.* **2024**, *4*, No. 200120.
(33) Walter, T. H.; Oldfield, E. Magic angle spinning oxygen-17 NMR of aluminum oxides and hydroxides. *J. Phys. Chem.* **1989**, *93*, 6744−6751.
(34) Mueller, K. T.; Wu, Y.; Chmelka, B. F.; Stebbins, J.; Pines, A. High-resolution oxygen-17 NMR of solid silicates. *J. Am. Chem. Soc.* **1991**, *113*, 32−38.
(35) Chen, J.; Wang, F.; Wen, Y.; Tang, W.; Peng, L. Emerging applications of ^{17}O solid-state NMR spectroscopy for catalytic oxides. *ACS Catal.* **2023**, *13*, 3485−3500.
(36) Du, J.-H.; Peng, L. Recent progress in investigations of surface structure and properties of solid oxide materials with nuclear magnetic resonance spectroscopy. *Chin. Chem. Lett.* **2018**, *29*, 747−751.
(37) Ashbrook, S. E.; Davis, Z. H.; Morris, R. E.; Rice, C. M. ^{17}O NMR spectroscopy of crystalline microporous materials. *Chem. Sci.* **2021**, *12*, 5016−5036.
(38) Bassey, E. N.; Reeves, P. J.; Seymour, I. D.; Grey, C. P. ^{17}O NMR spectroscopy in lithium-ion battery cathode materials: Challenges and interpretation. *J. Am. Chem. Soc.* **2022**, *144*, 18714−18729.
(39) Wang, M.; Wu, X.-P.; Zheng, S.; Zhao, L.; Li, L.; Shen, L.; Gao, Y.; Xue, N.; Guo, X.; Huang, W.; Gan, Z.; Blanc, F.; Yu, Z.; Ke, X.; Ding, W.; Gong, X.-Q.; Grey, C. P.; Peng, L. Identification of different oxygen species in oxide nanostructures with ^{17}O solid-state NMR spectroscopy. *Sci. Adv.* **2015**, *1*, No. e1400133.
(40) Wang, Q.; Li, W.; Hung, I.; Mentink-Vigier, F.; Wang, X.; Qi, G.; Wang, X.; Gan, Z.; Xu, J.; Deng, F. Mapping the oxygen structure of γ-Al_2O_3 by high-field solid-state NMR spectroscopy. *Nat. Commun.* **2020**, *11*, 3620.
(41) Merle, N.; Trébosc, J.; Baudouin, A.; Rosal, I. D.; Maron, L.; Szeto, K.; Genelot, M.; Mortreux, A.; Taoufik, M.; Delevoye, L.; Gauvin, R. M. ^{17}O NMR gives unprecedented insights into the structure of supported catalysts and their interaction with the silica carrier. *J. Am. Chem. Soc.* **2012**, *134*, 9263−9275.
(42) Li, Y.; Wu, X.-P.; Jiang, N.; Lin, M.; Shen, L.; Sun, H.; Wang, Y.; Wang, M.; Ke, X.; Yu, Z.; Gao, F.; Dong, L.; Guo, X.; Hou, W.; Ding, W.; Gong, X.-Q.; Grey, C. P.; Peng, L. Distinguishing faceted oxide nanocrystals with ^{17}O solid-state NMR spectroscopy. *Nat. Commun.* **2017**, *8*, 581.
(43) Wen, Y.; Zhang, W.; Wen, J.; Wang, F.; Ke, X.; Chen, J.; Peng, L. Tracking the facet transformation of CeO_2 by ^{17}O solid-state nuclear magnetic resonance. *J. Phys. Chem. Lett.* **2024**, *15*, 11587−11592.
(44) Peng, L.; Liu, Y.; Kim, N. J.; Readman, J. E.; Grey, C. P. Detection of Bronsted acid sites in zeolite HY with high-field ^{17}O-MAS-NMR techniques. *Nat. Mater.* **2005**, *4*, 216−219.
(45) Huo, H.; Peng, L.; Gan, Z.; Grey, C. P. Solid-State MAS NMR studies of Bronsted acid sites in zeolite H-mordenite. *J. Am. Chem. Soc.* **2012**, *134*, 9708−9720.
(46) Pugh, S. M.; Wright, P. A.; Law, D. J.; Thompson, N.; Ashbrook, S. E. Facile, room-temperature ^{17}O enrichment of zeolite frameworks revealed by solid-state NMR spectroscopy. *J. Am. Chem. Soc.* **2020**, *142*, 900−906.
(47) Peng, L.; Huo, H.; Liu, Y.; Grey, C. P. ^{17}O Magic angle spinning NMR studies of Brønsted acid sites in zeolites HY and HZSM-5. *J. Am. Chem. Soc.* **2007**, *129*, 335−346.
(48) Chen, J.; Hope, M. A.; Lin, Z.; Wang, M.; Liu, T.; Halat, D. M.; Wen, Y.; Chen, T.; Ke, X.; Magusin, P. C. M. M.; Ding, W.; Xia, X.; Wu, X.-P.; Gong, X.-Q.; Grey, C. P.; Peng, L. Interactions of oxide surfaces with water revealed with solid-state NMR spectroscopy. *J. Am. Chem. Soc.* **2020**, *142*, 11173−11182.
(49) Du, J.-H.; Chen, L.; Zhang, B.; Chen, K.; Wang, M.; Wang, Y.; Hung, I.; Gan, Z.; Wu, X.-P.; Gong, X.-Q.; Peng, L. Identification of CO_2 adsorption sites on MgO nanosheets by solid-state nuclear magnetic resonance spectroscopy. *Nat. Commun.* **2022**, *13*, 707.
(50) Song, B.; Li, Y.; Wu, X.-P.; Wang, F.; Lin, M.; Sun, Y.; Jia, A.-P.; Ning, X.; Jin, L.; Ke, X.; Yu, Z.; Yang, G.; Hou, W.; Ding, W.; Gong, X.-Q.; Peng, L. Unveiling the surface structure of ZnO nanorods and H_2 activation mechanisms with ^{17}O NMR spectroscopy. *J. Am. Chem. Soc.* **2022**, *144*, 23340−23351.
(51) Duncan, D. C.; Hill, C. L. Mechanism of reaction of reduced polyoxometalates with O_2 evaluated by ^{17}O NMR. *J. Am. Chem. Soc.* **1997**, *119*, 243−244.
(52) Gordon, C. P.; Engler, H.; Tragl, A. S.; Plodinec, M.; Lunkenbein, T.; Berkessel, A.; Teles, J. H.; Parvulescu, A. N.; Copéret, C. Efficient epoxidation over dinuclear sites in titanium silicalite-1. *Nature* **2020**, *586*, 708−713.
(53) Sun, T.; Xu, S.; Xiao, D.; Liu, Z.; Li, G.; Zheng, A.; Liu, W.; Xu, Z.; Cao, Y.; Guo, Q.; Wang, N.; Wei, Y.; Liu, Z. Water-induced

https://doi.org/10.1021/acsomega.5c00998
ACS Omega 2025, 10, 13655−13663

structural dynamic process in molecular sieves under mild hydrothermal conditions: ship-in-a-bottle strategy for acidity identification and catalyst modification. *Angew. Chem., Int. Ed.* **2020**, *59*, 20672−20681.
(54) Yang, C.; Wang, J.; Xia, X.; Ding, L.; Wen, Y.; Zhao, T.; Ke, X. K.; Gong, X.-Q.; Wu, X.-P.; Ding, W.; Peng, L. Can subsurface oxygen species in oxides participate in catalytic reactions? An ^{17}O solid-state nuclear magnetic resonance study. *J. Phys. Chem. Lett.* **2024**, *15*, 8218−8223.
(55) Li, Z.; Ji, S.; Liu, Y.; Cao, X.; Tian, S.; Chen, Y.; Niu, Z.; Li, Y. Well-defined materials for heterogeneous catalysis: From nanoparticles to isolated single-atom sites. *Chem. Rev.* **2020**, *120*, 623−682.
(56) Hu, Y.-Y.; Liu, Z.; Nam, K.-W.; Borkiewicz, O. J.; Cheng, J.; Hua, X.; Dunstan, M. T.; Yu, X.; Wiaderek, K. M.; Du, L.-S.; Chapman, K. W.; Chupas, P. J.; Yang, X.-Q.; Grey, C. P. Origin of additional capacities in metal oxide lithium-ion battery electrodes. *Nat. Mater.* **2013**, *12*, 1130−1136.
(57) Lee, H. C.; Oldfield, E. High-field oxygen-17 nuclear magnetic resonance spectroscopic observation of $^{17}O_2$ in Vaskas compound $IrCOXO_2PPh_{32}$; X = Cl, I and in PtO_2 PPh_{32}. *J. Magn. Reson.* **1986**, *69*, 367−370.
(58) Bayer, G.; Wiedemann, H. G. Formation, dissociation and expansion behavior of platinum group metal oxides (PdO, RuO_2, IrO_2). *Thermochim. Acta* **1975**, *11*, 79−88.
(59) Parker, S. F.; Robertson, S. J.; Imberti, S. Structure and spectroscopy of the supercapacitor material hydrous ruthenium oxide, $RuO_2 \bullet xH_2O$, by neutron scattering*. *Mol. Phys.* **2019**, *117*, 3417−3423.
(60) Meadows, M. D.; Smith, K. A.; Kinsey, R. A.; Rothgeb, T. M.; Skarjune, R. P.; Oldfield, E. High-resolution solid-state NMR of quadrupolar nuclei. *Proc. Natl. Acad. Sci. U.S.A.* **1982**, *79*, 1351−1355.
(61) Xue, X.; Stebbins, J. F.; Kanzaki, M. Correlations between ^{17}O NMR parameters and local structure around oxygen in high-pressure silicates: Implications for the structure of silicate melts at high pressure. *Am. Mineral.* **1994**, *79*, 31−42.
(62) Maekawa, H.; Florian, P.; Massiot, D.; Kiyono, H.; Nakamura, M. Effect of alkali metal oxide on ^{17}O NMR parameters and Si−O−Si angles of alkali metal disilicate glasses. *J. Phys. Chem.* **1996**, *100*, 5525−5532.
(63) Vermillion, K. E.; Florian, P.; Grandinetti, P. J. Relationships between bridging oxygen ^{17}O quadrupolar coupling parameters and structure in alkali silicates. *J. Chem. Phys.* **1998**, *108*, 7274−7285.
(64) Clark, T. M.; Grandinetti, P. J.; Florian, P.; Stebbins, J. F. Correlated structural distributions in silica glass. *Phys. Rev. B* **2004**, *70*, No. 064202.
(65) Trease, N. M.; Clark, T. M.; Grandinetti, P. J.; Stebbins, J. F.; Sen, S. Bond length-bond angle correlation in densified silica—Results from ^{17}O NMR spectroscopy. *J. Chem. Phys.* **2017**, *146*, 184505.
(66) Oldfield, E.; Coretsopoulos, C.; Yang, S.; Reven, L.; Lee, H. C.; Shore, J.; Han, O. H.; Ramli, E.; Hinks, D. ^{17}O nuclear-magnetic-resonance spectroscopic study of high-T_c superconductors. *Phys. Rev. B* **1989**, *40*, 6832−6849.
(67) Shen, L.; Wu, X.-P.; Wang, Y.; Wang, M.; Chen, J.; Li, Y.; Huo, H.; Hou, W.; Ding, W.; Gong, X.-Q.; Peng, L. ^{17}O solid-state NMR studies of ZrO_2 nanoparticles. *J. Phys. Chem. C* **2019**, *123*, 4158−4167.
(68) Narsimha Rao, E.; Vaitheeswaran, G.; Reshak, A. H.; Auluck, S. Role of spin−orbit interaction on the nonlinear optical response of $CsPbCO_3F$ using DFT. *Phys. Chem. Chem. Phys.* **2017**, *19*, 31255−31266.
(69) Alkan, F.; Dybowski, C. Spin-orbit effects on the ^{125}Te magnetic-shielding tensor: A cluster-based ZORA/DFT investigation. *Solid State Nucl. Magn. Reson.* **2018**, *95*, 6−11.
(70) Gómez-Ortiz, F.; Carral-Sainz, N.; Sifuna, J.; Monteseguro, V.; Cuadrado, R.; García-Fernández, P.; Junquera, J. Compatibility of DFT+U with non-collinear magnetism and spin-orbit coupling within a framework of numerical atomic orbitals. *Comput. Phys. Commun.* **2023**, *286*, No. 108684.
(71) Fernandez, C.; Bodart, P.; Amoureux, J. P. Determination of ^{51}V quadrupole and chemical shift tensor orientations in V_2O_5 by analysis of magic-angle spinning nuclear magnetic resonance spectra. *Solid State Nucl. Magn. Reson.* **1994**, *3*, 79−91.
(72) Shore, J. S.; Wang, S. H.; Taylor, R. E.; Bell, A. T.; Pines, A. Determination of quadrupolar and chemical shielding tensors using solid-state two-dimensional NMR spectroscopy. *J. Chem. Phys.* **1996**, *105*, 9412−9420.
(73) Wu, A.; Cremer, D.; Gauss, J. ^{17}O NMR chemical shifts of polyoxides in gas phase and in solution. *J. Phys. Chem. A* **2003**, *107*, 8737−8745.
(74) Hart, R. T., Jr.; Zwanziger, J. W. ^{17}O NMR spectroscopy of α-TeO_2 and Na_2TeO_3. *J. Am. Ceram. Soc.* **2005**, *88*, 2325−2327.
(75) Kong, X.; Terskikh, V. V.; Khade, R. L.; Yang, L.; Rorick, A.; Zhang, Y.; He, P.; Huang, Y.; Wu, G. Solid-state ^{17}O NMR spectroscopy of paramagnetic coordination compounds. *Angew. Chem., Int. Ed.* **2015**, *54*, 4753−4757.
(76) Hope, M. A.; Halat, D. M.; Lee, J.; Grey, C. P. A ^{17}O paramagnetic NMR study of Sm_2O_3, Eu_2O_3, and Sm/Eu-substituted CeO_2. *Solid State Nucl. Magn. Reson.* **2019**, *102*, 21−30.
(77) Massiot, D.; Fayon, F.; Capron, M.; King, I.; Le Calvé, S.; Alonso, B.; Durand, J.-O.; Bujoli, B.; Gan, Z.; Hoatson, G. Modelling one- and two-dimensional solid-state NMR spectra. *Magn. Reson. Chem.* **2002**, *40*, 70−76.
(78) Kresse, G.; Hafner, J. Ab initio molecular-dynamics simulation of the liquid-metal–amorphous-semiconductor transition in germanium. *Phys. Rev. B* **1994**, *49*, 14251−14269.
(79) Perdew, J. P.; Burke, K.; Ernzerhof, M. Generalized gradient approximation made simple. *Phys. Rev. Lett.* **1996**, *77*, 3865−3868.
(80) Blöchl, P. E. Projector augmented-wave method. *Phys. Rev. B* **1994**, *50*, 17953−17979.
(81) Sundholm, D.; Olsen, J. Finite element multiconfiguration Hartree-Fock calculations on carbon, oxygen, and neon: the nuclear quadrupole moments of ^{11}C, ^{17}O, and ^{21}Ne. *J. Phys. Chem.* **1992**, *96*, 627−630.

https://doi.org/10.1021/acsomega.5c00998
ACS Omega 2025, 10, 13655−13663